Chapter 3

Endogenous Second Harmonic Generation in Zebrafish

One emerging technique for biological imaging is harnessing nonlinear optics to probe endogenous structures [67, 68, 69, 70, 71, 72, 73, 74, 75, 76]. The vast majority of an organism is constituted of proteins and water. Water has an index of refraction of 1.33, while tissue has an index of approximately 1.4 [77, 78, 79]. The makes living tissue nearly optically continuous, compared to the optical contrast between tissue and gold, for instance. How does one then optically study objects of interest in such a low-contrast environment? Of course, the most common approach to selective imaging is to introduce something to enhance this contrast, such as a stain or fluorescent dye. Fluorescent dye, in particular, allows for exceptional contrast, because the only source of light at the desired wavelength will be from dye and low-level natural endogenous autofluorescence. However, the natural chirality of proteins can serve as a source of second harmonic generation, allowing us to distinguish highly ordered structures from the amorphous background without introducing any foreign components. That is, only certain structures will transform two photons from the input laser into one

photon at half the wavelength. Detecting the SHG wavelength will then allow for localization of the source structures. For example, the ordered arrangement of muscles and collagen serve as particularly bright sources of biological SHG, shown in figure 3.1 for the case of muscle. There are also a number of studies of SHG and hyper-Rayleigh scattering from films and suspensions of proteins and DNA [80, 81, 82]. SHG has two drawbacks. First, the probability of two photons combining is very small, so the input laser must be very powerful. Second, unlike fluorescence, where a material absorbs light and reemits it in a wavelength characteristic of that dye, SHG is defined as the doubling of the laser frequency, so all sources of SHG will appear identical without further characterization. Often, just the morphology of the object is sufficient to distinguish, for example, myosin from collagen, as in figure 3.4. However, this is not an ideal approach, nor does it leverage the strengths of SHG. By better understanding the process of SHG production, we can identify how SHG from one type of tissue would be unique, whether it be an emission direction, polarization, or intensity specific to the structures in question.

To this end, we investigate the wavelength dependence of SHG from zebrafish (*Danio rerio*) muscle. We measure the SHG from regions of the muscle and characterize the resulting spectrum. In addition, we identify some the of characteristics of SHG imaging distinct from fluorescence imaging. The organism in question is a common subject in optical microscopy due to a number of favorable factors, such as: its genome is sequenced, it can be induced to be highly transparent, it matures rapidly, among other practical reasons for its use as a model organism. Therefore, our

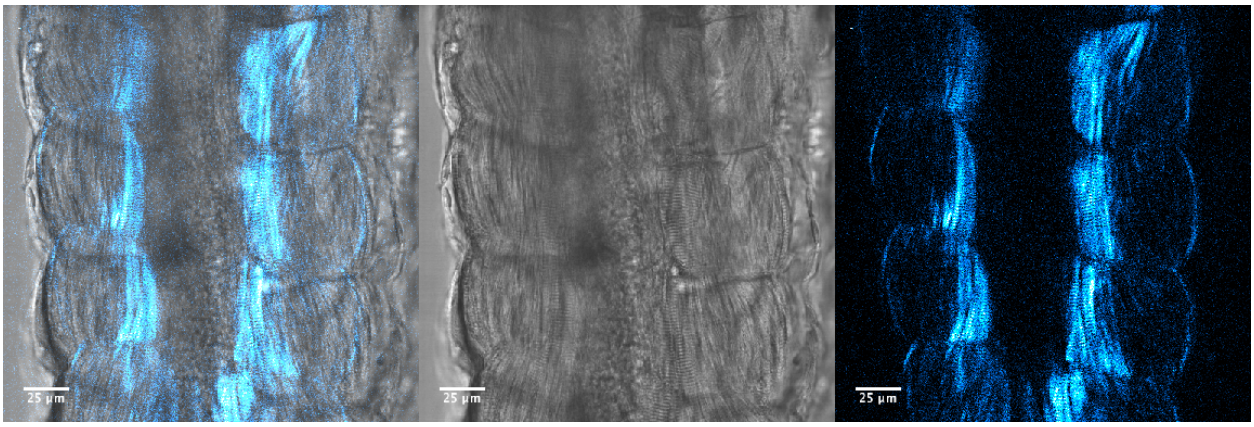

Figure 3.1: Sagittal section of zebrafish 36 hours post fertilization. Left, composite brightfield and transmitted SHG. Center, brightfield. Right, transmitted SHG. Scale bar is 25 microns.

conclusions will be specific to muscle from zebrafish, but most of it is transferrable to images of other organisms.

Muscle in zebrafish are organized into chevron-shaped somites, as shown in figure 3.3. The muscle surrounds a central notochord, which bisects figure 3.3. This image illustrates one of the central attractions of second harmonic generation as an imaging modality. Without any artificial or genetically encoded labels, zebrafish still produce significant autofluorescence, but fluorescence has very small overlap with the SHG wavelength. In addition, fluorescence is radiated isotropically, while muscle SHG is coherently forward directed [84]. There have been a number of studies of wavelength dependence of SHG in proteins [85, 86, 87] but none in muscle, with its unique microscopic structures (see section 3.1.1).

There are a number of factors that could contribute to wavelength dependence. The SHG produced at a point is given by $P^{(2)}(x) = \chi^{(2)}(\omega, \mathbf{x}) : \mathbf{E}(\omega, \mathbf{x})\mathbf{E}(\omega, \mathbf{x})$, where $\chi^{(2)}$ is the SHG susceptibility and $\mathbf{E}$ is the incident electric field vector. From direct

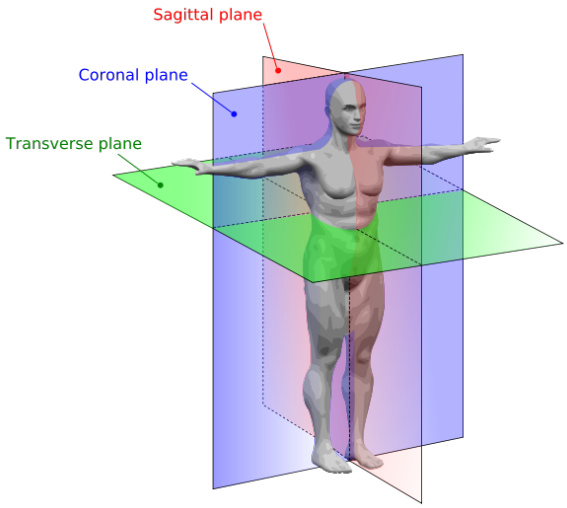

Figure 3.2: Anatomical planes. Zebrafish are oriented laterally, meaning the sagittal plane is parallel to the ground and perpendicular to the laser. Image from [83].

inspection, it is clear that wavelength dependence could originate from the susceptibility itself, which would be due to the underlying material properties of the protein. The incoming electric field will vary in power, which is part of a greater wavelength dependent instrument response. Last, there could be variation in the efficiency of SHG production due to phase-matching, resulting from the underlying crystalline structure of the muscle. It is this last point that suggests possible diagnostic applications of the wavelength dependence of SHG, as there are a number of disorders, namely muscular dystrophy [88], which alter the underlying crystalline structure [89].

3.1 Structure of Muscle

3.1.1 Muscle Construction

Muscle, in particular, is an excellent candidate for biological SHG susceptibility, because it possess a high degree of spatial order. To facilitate gross movement in an

Figure 3.3: Label-free image of fixed zebrafish embryo, sagittal section. Scale bar is 50 microns. Green is autofluorescence from the fish and the fixative, blue is transmitted SHG. Fish is 36 hours post-fertization.

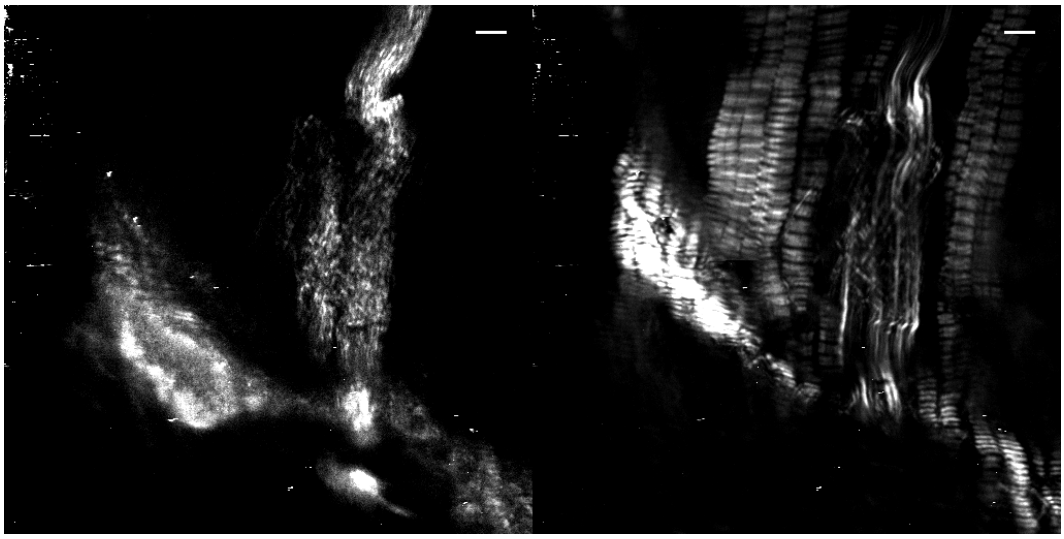

Figure 3.4: Second harmonic generation from muscle and collagen. Image is a sagittal section from the end of a zebrafish tail. Left: Epi collected emission. Collagen are the wispy lines in the middle running vertically. The horizontal streaks are luminescence from laser damage. Right: Trans collected emission. Again, collagen are the wispy lines in the middle, while muscle are the striated ribbons to either side. Exclusively trans-directed SHG is characteristic of muscle. Image taken with 100x α-Plan-Apochromat 1.46NA. Scale bar is 5 microns.

organism, it must be organized in a way to allow it to coordinate the molecular motions of proteins across the entire muscle. In general, muscle fibers are organized on the molecular level as a lattice of parallel protein filaments, including the force generating and scaffolding components, myosin and actin, respectively. Myosin, a molecular motor, pulls on the actin, and, due to long-range correlation of the activation of the myosin, this results in muscle contraction. The myosin and actin are packaged in periodic longitudinal units called sarcomeres, shown in figure 3.5. The myosin are tied together in the center of the sarcomere, called the M-line [90], while the actin anchoring positions are Z-lines, as in figure 3.5. The region of the sarcomere containing the myosin appears optically distinct, and is called the A-band. The myosin is also loosely bound on both sides to the Z-lines via titin, a spring-like protein,

maintaing its position in the center of the sarcomere and maintaining an equilibrium resting distance between the Z-lines. When activated, the myosin ratchets against the actin, pulling neighboring Z-lines closer together.

Myosin and actin are arrayed in hexagonally packed filaments called myofibrils [91], with the protein arranged with a characteristic spacing between myosin filaments of 40 – 50 nm [92, 93, 94, 95]. This packing is illustrated in figure 3.6. That is, the lattice vectors observed by x-ray diffraction are consistent with hexagonal Fourier amplitudes of $K_{nm} \propto a^{-1}\sqrt{(n^2+m^2+mn)^{-1}}$, where the lattice spacing is the characteristic length of a = 40–50 nm, depending on the contractile state of the fiber [94, 96, 95][1]. The hexagonal packing has also been clearly observed in TEM micrographs [91, 92]. Each myofibril is approximately 1 μm across. Myofibrils are in turn packed into myocytes, the cellular units of muscles, which are about 10 μm across [97, 92].

The myosin and actin are packed with high regularity within the myofibril, and the myofibrils are highly aligned with their neighbors [98], shown in figure 3.5, and this regularity contributes to strong production of SHG. Although both the myosin and actin fibers are highly ordered, it is known that SHG only originates from the myosin, based on complimentary staining [99, 100, 101] and on mutating myosin to reduce SHG [102, 103]. Depending on the contractile state of the muscle fibrils, the sarcomere spacing will have differing myosin spacings [100, 104, 105, 96]. The longer the sarcomeric unit, the smaller the myosin spacing [93, 96]. In addition, muscle

[1]It appears the actin are anchored to the Z-line in a square lattice, while the myosin are held at the M-line in a hexagonal lattice. So, close to the Z-line, the packing will be dominated by the square-lattice of the rigidly held actin [92, 93].

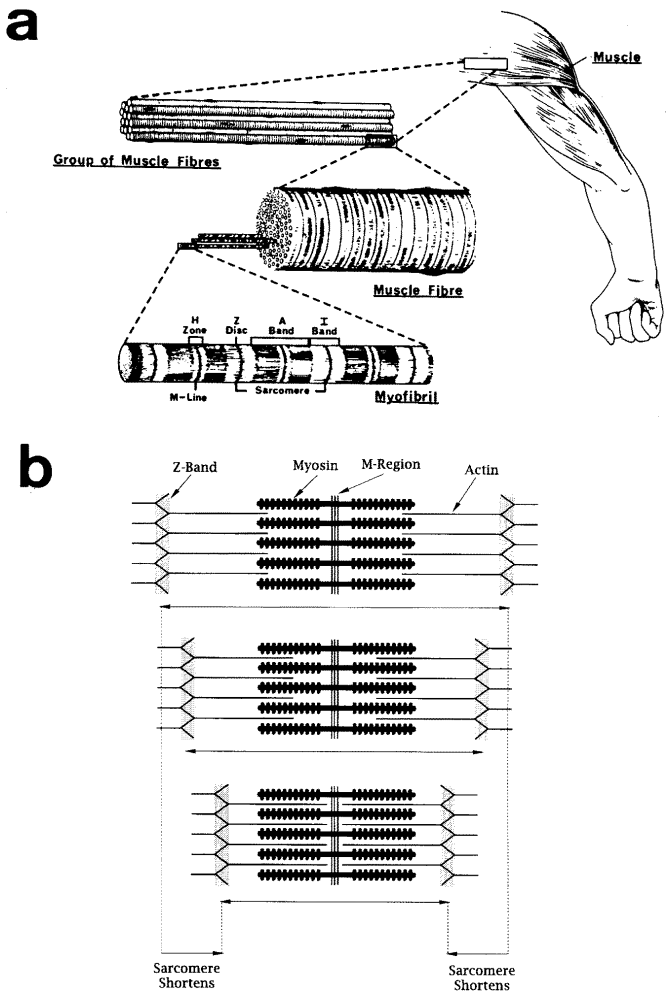

Figure 3.5: (a) A multiscale illustration of muscle organization, and (b) a cartoon of the process of muscle contraction. Missing from this cartoon is the fact that the myosin spacing grows as the sarcomere compresses [93]. Image is from [107].

contraction is driven by the conformation transition of the myosin molecular motor, which causes the relative angle of the asymmetric units to change with respect to the myofibril axis [106]. It has been hypothesized that when at rest, the myosin tails at the M-line are packed together in a way that cancels inversion asymmetry, possibly causing contraction dependent SHG [105]. These distances and angles determine the degree of the second harmonic generation, so we expect some heterogeneity in images of muscle, but they will all retain the same basic patterns.

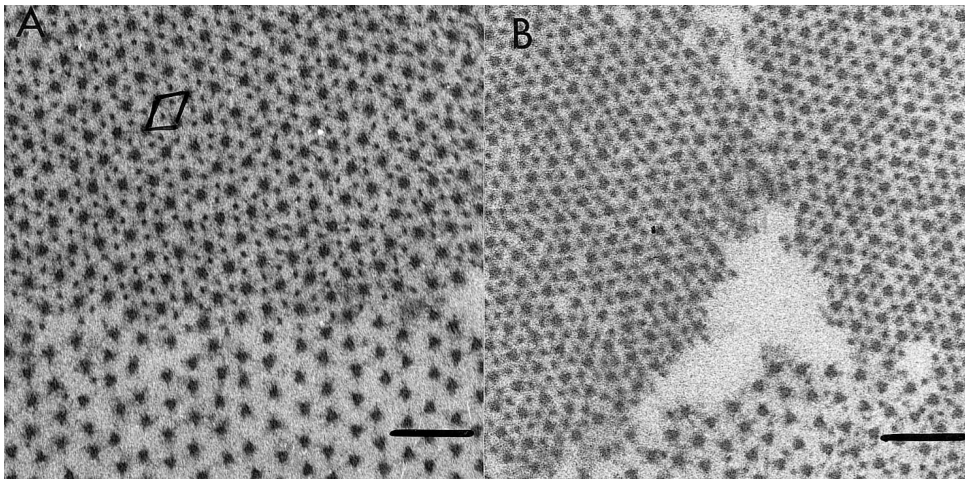

Figure 3.6: TEM micrographs of myofibril crosssection, showing hexagonal packing of myosin and actin. Myosin are the larger dots, while actin are smaller dots. (a)Relaxed fibrils. The bottom portion of both images is a portion of a fibril with only myosin, e.g., near the M-line. (b) Contracted fibrils. The scale bar is 100 nm. From [93].

3.1.2 Optical Properties of Muscle

The regularity in myofibrils carries over into its optical properties. Because of the underlying chirality of the proteins, myofibrils have well documented birefringence [108, 109, 110], meaning the muscle has a fast (ordinary) and slow (extraordinary) axis. The optical axis, e.g., the slow axis, is parallel to the myosin filaments [108]. The birefringence is defined as the difference between the refractive indices $B = n_e - n_o$, corresponding respectively to the extraordinary and ordinary axes. More specifically, observations show $B = 2 \cdot 10^{-3}$ [108, 110]. In addition, this birefringence has been observed to change systematically and approximately linearly with the length of the sarcomere or, conversely, with the density of myosin thick filaments, where birefringence increases by up to a factor of two between a relaxed sarcomere and one in contraction [108]. The birefringence has a number of origins. First, there is the underlying chirality of the protein, or more specifically, an intrinsic birefringence due to

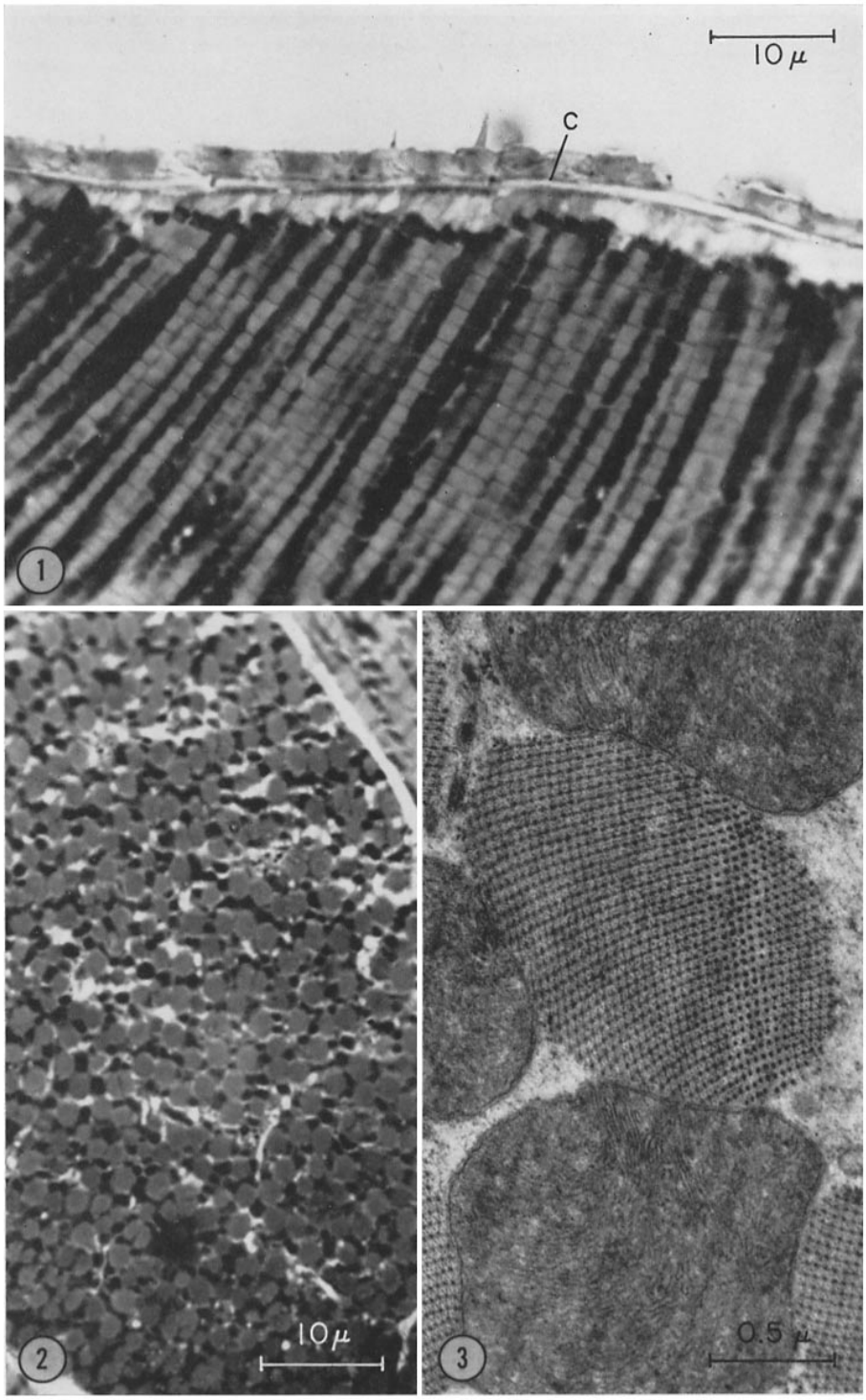

Figure 3.7: (1) A longitudinal section of muscle, showing myofibrils, light striped bands, and mitochondria (dark objects between myofibrils). The Z-lines (dark lines), and to a lesser extent, the A-band and M-lines (lighter lines) are visible. (2) A crosssection of the same muscle, showing individual myofibrils packed in a quasi-crystalline manner within the larger cell. (3) Close-up of a single myofibril, with myosin stained as dark dots. Image is from [92].

asymmetric polarizability of the underlying electrons, and a change in the underlying protein structure, such as conformational motion of the myosin heads, would alter the birefringence to some degree. Second, there is form birefringence, originating from the highly asymmetric cylindrical protein filaments. The aligned filaments cause the material to appear to have different character depending on the polarization of light, were a liquid crystal. As sarcomeres contract, their myosin filaments increase their separation (an observed conservation of volume [93]), and this drives a change in the birefringence. Both types of birefringence combine to alter the production of SHG, primarily due to spatial beam walk-off, which limits the effective interaction length of the focused laser [111, 112], and also due to coupling between the ordinary and extraordinary directions [113]. It has been estimated that form birefringence accounts for approximately 70% of the total birefringence [108]. In addition to birefringence, the order in myofibrils also gives rise to optical Bragg diffraction. This is present on the nanometer-scale, where the ordered protein can be studied by x-ray crystallography *in vivo* [95], and it is also present on the micron scale, where optical diffraction is used to study sarcomere structure [114, 115, 116]. Bragg diffraction affects phase-matching conditions, which are vital to determining the efficiency of SHG conversion, as will be shown in section 4.2.2.

A second major influence on the second harmonic generation is the wavelength-dependent index of refraction. The refractive index of tissue has been explored in a number of contexts [117, 77, 118, 79, 119, 78]. Pure protein has a refractive index of 1.5 – 1.6 [78], but myofibrils have a hexagonal lattice of tightly packed heteroge-

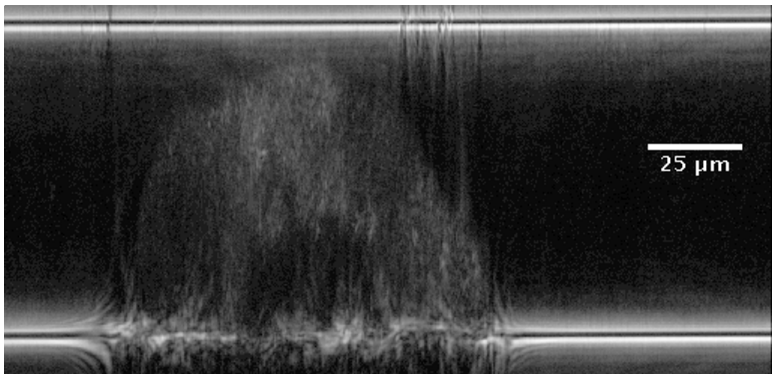

(a) Reflection intensity

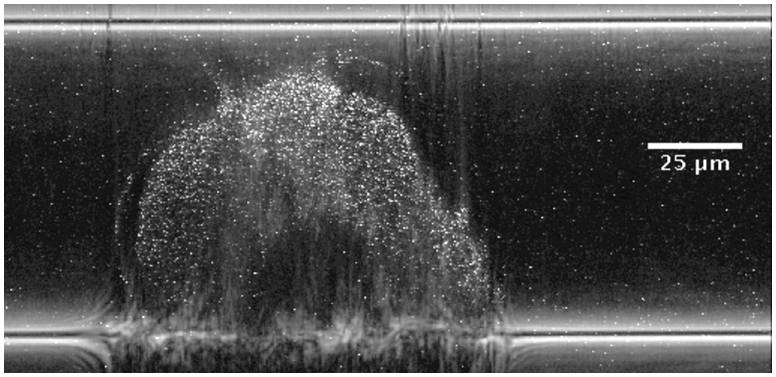

(b) Reflection intensity with endogenous fluorescence overlay

Figure 3.8: Reflection of 850 nm laser pulses indicates the optical density of the zebrafish transverse section. Laser originates from the top of the image. The refractive index heterogeneity of the zebrafish muscle and neural tube causes significant optical aberration, realized as the distorted boundary between the fish and the glass, at the bottom of the images. The top band and bottom bands are the boundary between the gel holding the section and the glass coverslips.

nous protein, and it will have an effective index that is a combination of protein and water. Techniques measuring an average index report a characteristic index of 1.4 [79, 118, 119]. Tissue-specific variations cause the index to vary by 10%. For example: epidermis is 1.44, dermis is 1.4, and the outmost layer of skin, the stratum corneum, is 1.55 at 650 nm [77, 119]. Attempts to measure the refractive index of a 5-day old zebrafish by measuring the optical thickness of the sample using the Ti-Sapphire laser [118] were stymied by the optical heterogeneity of the muscle, shown in figure 3.8. Because tissue, in particular myofibrils, has no electronic resonances in the visible wavelengths, their refractive properties obey the general relation of normal dispersion, where the refractive index increases with increasing frequency. Indeed, Ding et al. [119] and Andersen and Nir [78] find wavelength dependent refraction indices well described by the Cauchy and Lorentz-Lorenz dispersion relations, respectively. Works that investigate the polarization dependence of the refractive index of ovine and porcine muscle find results consistent with the previous birefringence mentioned above [77]. Hence, the index dependence of muscle will have a simple monotonically decreasing functional form given by the Cauchy dispersion relation. In this work, we take the wavelength-dependent refraction indexes for porcine muscle, as measured by Cheng et al. [120] and reported by Bashkatov et al. [77]. Fitting their data to a Cauchy dispersion gives an refractive index for muscle across the entire relevant spectrum:

$$n(\lambda) = \sqrt{2.116 + \frac{22.45\lambda^2}{\lambda^2 - 53.9343}}. \tag{3.1}$$

where λ is expressed in microns.

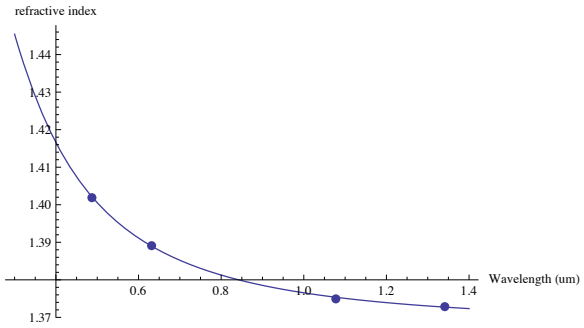

Figure 3.9: Using experimentally measured refraction index data from porcine muscle [120] (total internal reflection), we determine the refractive index across the entire spectrum. Points are experimental data, line is fit by eq. (3.1).

3.2 Methods for Measuring Second Harmonic Generation

All zebrafish, unless noted, were embedded in 1% or 2% low-melting agarose with 30% w/v Danieau buffer for imaging. After fertilization, the embryos are transferred in a petri dish to a 28 degree incubator in egg water. The fish grow for 24 hours, and then pheynl-thio-urea (PTU) is added (0.003% w/v) to inhibit pigment formation. After the desired amount of maturing time elapsed, fish were anesthetized in 0.015% tricaine. For fixing, the fish were immersed in 4% PFA at room temperature for 45 minutes. They were washed on a nutator for 20 minutes three times in Ca-Mg free PBS 1x. They were stored at 4 °C until needed. Live fish were anesthetized and immediately laterally embedded in agarose containing 0.015% tricaine.[2] Two-well #1 cover-slips (Lab-Tek, Nalge Nunc International) were used to contain the samples. Although no live samples are presented here, they do not produce SHG that is noticeably different from fixed fish.

[2]All fish preparation protocols were conducted and refined by Bill Dempsey.

Fish were oriented in the gel to maximize resulting SHG, which depended on the polarization of the microscope laser, i.e.,the laser field was oriented away from the central myosin-actin axis [121, 101]. Imaging took place at the House Ear Institute's Zeiss 710 LSM Confocor 2. The laser was a Coherent Chameleon Ultra II Ti-Sapphire 140-fs pulsed laser. Laser power was selected to be approximately 60 mW at the back aperture to the objective, which was determined by wavelength corrected power meter. Imaging was done with Zeiss objectives which were corrected for UV-VIS-IR imaging. All images were taken with the 25x LD LCI "Plan-Apochromat" 0.8 Imm Corr DIC unless noted otherwise. The correction collar was used to optimize point spread function at each wavelength, using either Dark Red Quantum Dots from NN-labs, Inc. or luminescent debris from Zebrafish skin to find point spread functions. Given 60 mW at the back aperture, this leads to average power densities of approximately 10 MW/cm^2, and peak power densities[3] of 10^{11} W/cm^2. All SHG was trans-imaged, using a 0.5 NA condenser to collect the light. The laser was filtered with a Semrock 680/SP short-pass filter, and the SHG was selected using a Semrock 417/60 bandpass filter. To obtain wavelength-corrected images, the wavelengths between 780 nm and 890 nm were used in 10 nm intervals, and the laser power was corrected to bring the power at the back aperture of the object as close to 60 mW as possible. After collection, the images were computationally corrected for objective transmission, condenser transmission, and PMT sensitivity. Images were not corrected for short-pass or bandpass filter transparency due to the small variation across the spectrum. The correction collar of the 25x was used to obtain an optimal point

[3]Reported from `http://www.coherent.com/downloads/ChameleonUltraFamily_DS_0510.pdf`.

spread function. However, the collar was not adjusted for each wavelength, primarily because manually adjusting the collar disrupted the sample alignment, and because the 0.8 NA objective had small wavelength dependent deviation in the focus, shown in figure 3.11. In addition, spectra did not differ systematically with collar adjustment.

To prepare morphant fish to recapitulate the phenotype of fish with Duchenne muscular dystrophy [122], a morpholino[4] sequence targeted to the *dmd* gene locus was injected into the yolk of zygote-stage zebrafish. The injection was 2.3 nL at a concentration $\sim$2.174 ng/μL, using a nanoject II Auto-nanoliter injector. Morphant fish which developed to 5 days were screened and prepared for imaging as above.

To visualize cell membrane and nuclei locations within the somite compartment, we used a transgenic zebrafish, which was a bistronic line coexpressing membrane-targeted cerulean fluorescent protein and a fusion H2B-Dendra2 fluorescent protein, targeted to the nucleus.[5] A founder of the line was crossed with an AB line wild-type [123]. The larvae were screened at 24 hours post fertilization for fluorescence and, if positive, prepared as above.

Laser damage proved to be the primary obstacle to optimizing images at every wavelength. As shown in figure 3.13, cells are easily damaged by two-photon laser pulses. Damage is not uniform, but it appears to be nucleated at bubbles or other optical heterogeneities. Once damage forms, the bubble grows larger and larger with each subsequent scan. Although the bubble may shrink over time, a permanent lesion

[4]Morpholinos are synthetic nucleic acid polymers designed to bind to mRNA and prevent the translation of the protein coded by specified target sequence. `http://en.wikipedia.org/wiki/Morpholino`

[5]Dempsey et alf in preparation

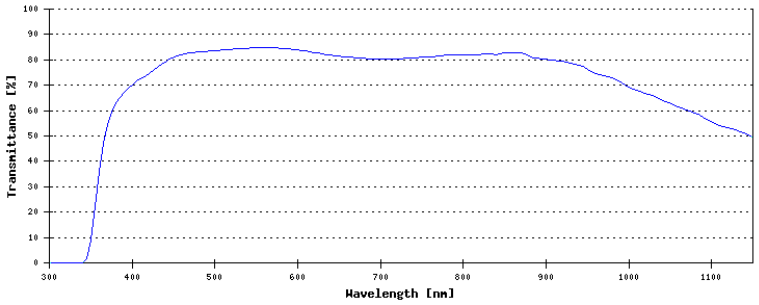

(a) Zeiss LD C-ApoChromat 25x 0.8 NA

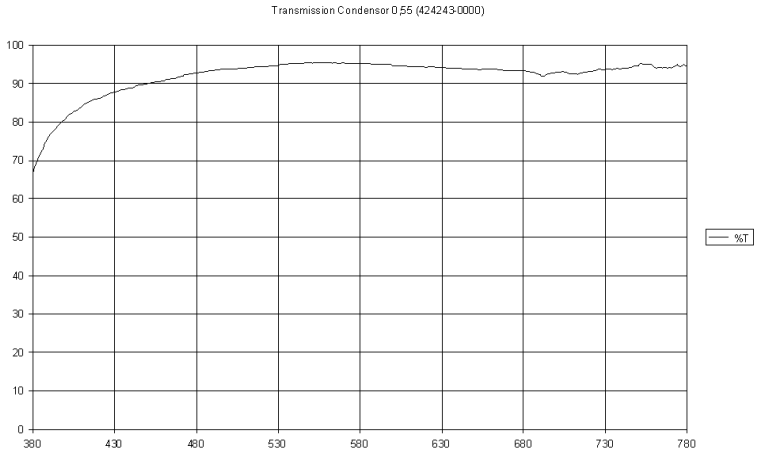

(b) Zeiss 0.5 NA Condensor

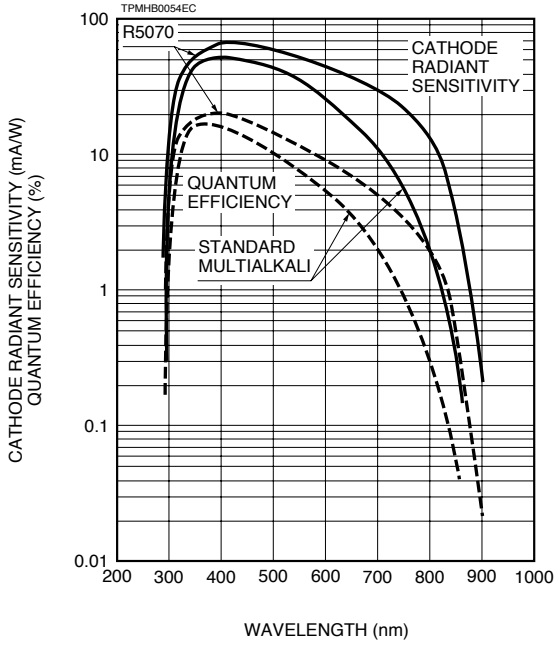

(c) Hamamatsu R5070 PMT

Figure 3.10: Each element of the imaging pathway has different wavelength dependent transmission or sensitivity. These characteristic spectra provided by the respective vendors were used to correct the signal.

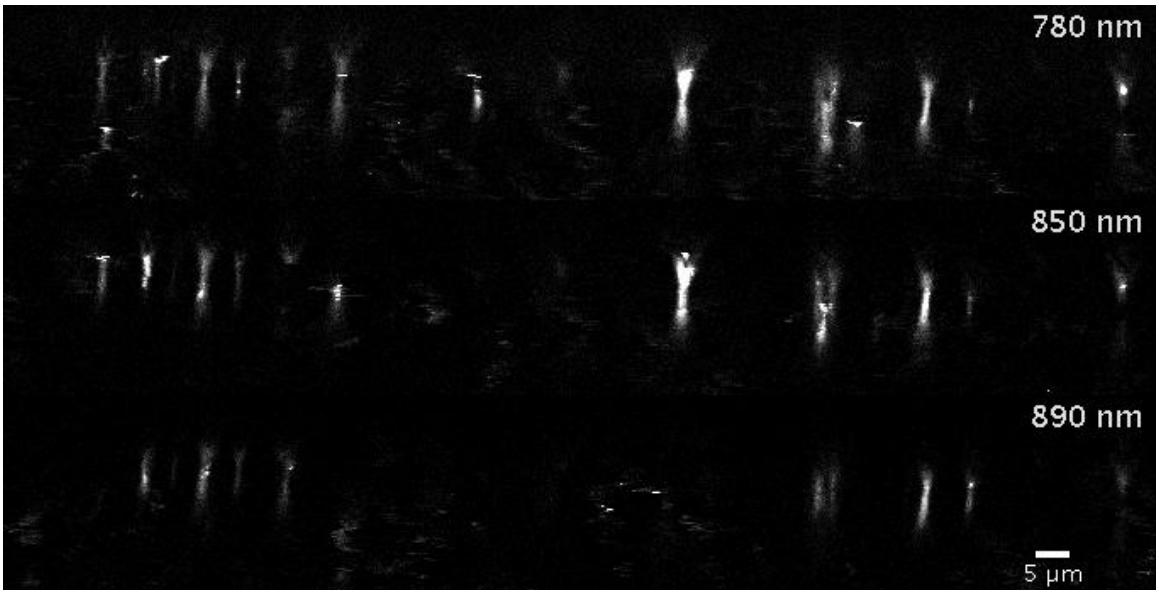

Figure 3.11: Fluorescent debris from the zebrafish were used to measure point spread functions at 790 nm, 850 nm, and 890 nm, using 25x 0.8 NA

remains.[6] Broadband emission from the damage sites is suggestive of laser-induced breakdown [124, 125] and self-steeping into supercontinuum generation [126, 127, 128]. In addition, fish need to be treated with 1-phenyl 2-thiourea (PTU) during embryogenesis to suppress the formation of pigmented cells such as melanocytes. Melanin is strongly absorbing, and irradiation leads to the formation of sufficient free radicals to initiate rapid laser damage and ablation. In addition, the broadband luminescence from pigment competes with SHG, confusing image interpretation, as shown in figure 3.12. Even with limited pigment, damage may still readily occur. As a result, power and observation times were limited.

Because of chromatic dispersion, the focus of the laser varies in depth as the

[6] Although the peak power of the laser at 25x, 0.8 NA is 10^{11} W/cm^2, self-focusing and near-field enhancements can easily elevate peak electric fields to near breakdown levels, 10^{15} W/cm^2. This is likely why damage nucleates at bubbles, lesions, and pigment (a source of free radicals). In addition, this makes imaging with 100x and other high NA objectives difficult to achieve without extreme damage to the sample.

Figure 3.12: An image of second harmonic generation from morphant zebrafish, optically sectioned along the sagittal plane. The speckling along the central neural tube is broadband luminescence from pigment cells. Lesions are evidenced by the circular outlines of luminescence. The microspeckling in the luminescence is due to rapid changes in the substrate, which are faster than the laser pixel dwell time, 1.56 μs. Scale bar is 50 microns.

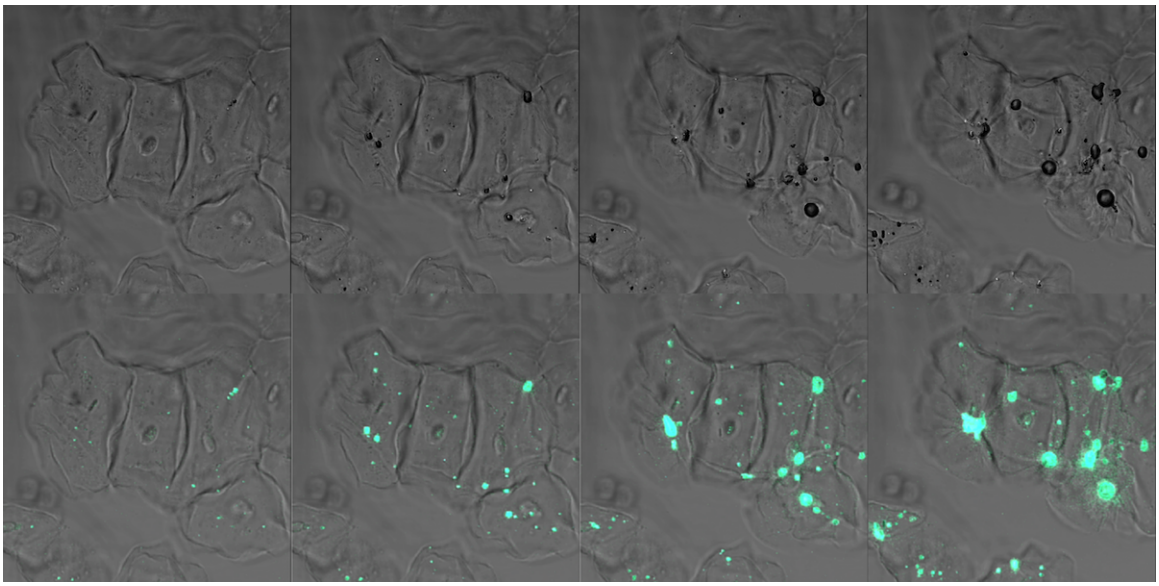

Figure 3.13: Epithelial cells accumulate damage over a 2 minute exposure to 820 nm Ti-Sapphire laser pulses, 10% power. The signature of the damage is broadband radiation, extending over the entire visible spectrum. The damage appears to be nucleated in tiny bubbles. The bubbles grow over time, ultimately tearing the cell. Upper Row: Transmitted laser light, Lower Row: Transmitted light plus false-color epidetected luminescence.

wavelength is tuned. The deviation in the depth of the focus between an image taken with the laser wavelength 780 nm and at 890 nm is over 1 μm, which is the width of a myofibril. Therefore, an image at 790 nm often contains myofibrils not in an image at 890 nm, and vice versa. To overcome this complication, images were taken in large "z-sections," or coronal slices, meaning the objective was stepped along the axis of laser propagation to image lines in multiple focal planes. Because the imaging resolution in the z-axis is well over a micron, taking 0.35 μm slices allowed all of the muscle to be captured. However, as mentioned in the last paragraph, exposure time needed to be limited to avoid complete ablation of the sample before all wavelengths could be imaged. As a result, only a 2D image was taken, with one axis in the z-direction (parallel to the laser propagation) and another axis perpendicular to the laser, chosen

to capture a region of interest but not necessarily with any specific orientation with respect to the fish or muscle. Variations in muscle fiber alignment within the somites cause there to be few preferred directions, allowing selection of planes which provide best imaging conditions.

3.3 Discussion

3.3.1 Representative Images

figure 3.15 shows a representative image of second harmonic generation from a 5-day old wildtype zebrafish. The muscle is clearly packed into chevron-shaped somites, and the dark Z-lines stand out in stark contrast with the bright A-bands. The myocytes contain highly aligned domains of tightly packed myofibrils [98], although the fish is too young for the muscles to develop to a state of full compaction. We a level of organization between the 1 μm myofibrils and the 10 μm myocytes that has not been well documented in the literature. The intensity of the SHG varies significantly across the muscle, corresponding to fluctuations in density and alignment. Although the individual myofibrils are not readily apparent, they can be recognized at the boundaries of the somites as the discrete steps, as seen on TEM in figure 3.7. Their width of approximate 1 micron is sufficient to resolve at this resolution, but their tight packing and close alignment with neighboring myofibrils makes distinguishing individuals difficult, but not impossible. Sometimes myofibrils are separated sufficiently to resolve individual fibers, even while in alignment with their neighbors, as

shown in figure 3.14. Because SHG comes from the dense myosin filaments within the sarcomeres, diagrammed in figure 3.5(a), we can interpret the dots in figure 3.14 to be myosin filaments radiating from the M-line. Because oppositely aligned myosin meets at the M-line, it is not a source of SHG, and this will be discussed further in section 4.3. The Z-lines are also dark, because they lack myosin completely. Hence, we observed the expected double lobed pattern in each sarcomere. This is a common motif observed in other studies that have isolated single myofibrils [129, 101].

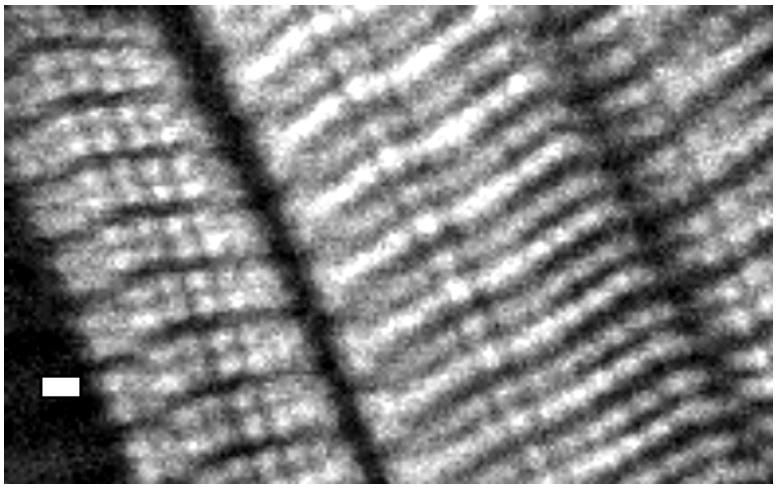

Figure 3.14: Close-up view of discrete structure of myofibrils. The Z-lines are dark, and the M-lines are dark. However, the M-lines are sandwiched between the A-bands, where myosin filaments produce SHG (see figure 3.5). Scale bar is 1 micron.

Another common motif is an interlocking herringbone pattern, as in figure 3.16. Others have observed these patterns, calling them "verniers" [99, 89] or "pitchforks" [100]. Their cause is unknown, although Recher et al. attribute them to maturing myofibrils [100]. When we look at the same muscle from two perpendicular planes, as in figure 3.7, we see these patterns appear where myocytes and small bundles of myofibrils come in close proximity. Because myosin runs parallel to the membrane, no SHG producing structures cross the membrane. However, figure 3.17

Figure 3.15: Second harmonic generation from wildtype. The section is along the sagittal plane. Scale bar is 50 microns.

shows the herringbone pattern crossing the fluorescent signal from the membrane, indicating that the herringbone pattern is an optical artifact, not a physical structure. Friedrich et al. observed a "vast increase" in vernier pattens in dystrophic mutants [89], which can be explained by the relative increase in disordered myofibrils [130], allowing more crossing within the imaging plane, leading to an apparent increase in subsequent vernier patterns. This will be more closely explained in section 4.3.

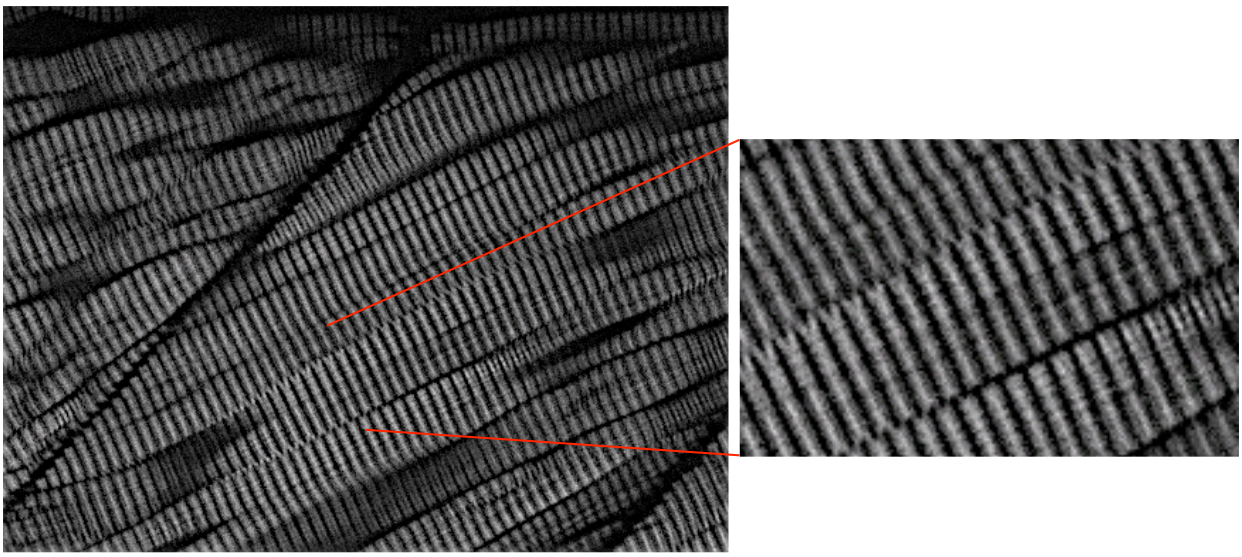

Figure 3.16: Inset shows magnified view of herringbone or "vernier" pattern from a 7 day post-fertilization zebrafish.

Morphant muscles show the same motifs as the wildtype muscles, which is to be expected because dystrophic disorders affect the structural reinforcements and anchoring components of the muscle [122, 131], and not the internal packing of the sarcomeres.[7] The myofibrils of morphant fish show significantly more flexibility and disorder, illustrated in figure 3.19. As morphants age, the myofibrils tear away from

[7]However, there is an inherent selection bias in this statement, as once the the structural integrity of the myofibrils are compromised to the point of disrupting the myosin lattice, the fish will be at or near death. We only studied live fish (or fixed live fish).

each other, losing muscle integrity due to a lack of sufficient dystrophin expression linking the interior of the muscle cells to the exterior. This work only deals with 5-day old morphants, leaving open the possibility that older morphants could differ in their SHG signature. Although this would not necessarily be useful diagnostically, because the morphant would be readily identifiable by the morphological degradation, it may help isolate the source of SHG spectra. Also, but not readily apparent from the images in this thesis, morphant SHG is substantially dimmer. Images in this work have been contrast-brightness corrected to be as easy to visualize as possible.[8] In addition, figure 3.19 shows that morphants contain disordered muscle interspersed with highly ordered muscle, leading to images with high dynamic range. figure 3.19 and figure 3.20 also reveal that myofibrils appear to be organized into larger bundles around 5 μm wide, something not well documented in the literature, but perhaps best documented by Sanger et al. [132].

3.3.2 Wavelength-Dependent SHG

Properly wavelength corrected images proved to be difficult to obtain, mostly because of the limited exposure time possible before the laser destroyed the sample. However, the protocols outlined in section 3.2 enable measuring a wide spectrum from 780 nm to 890 nm at 10 nm intervals. figure 3.21 shows representative results for a wildtype 5-day old fish. Because each point in the slice, Fig 3.21(a), has a different myofibril alignment and intensity, there are a number of ways to analyze the results. Absolute

[8]The only image alterations done on the images in this thesis were standard contrast and brightness adjustments along with cropping out regions of interest.

intensities are not reliable because too may factors alter the amount of laser power being delivered to a given point and the fraction of SHG that arrives that the detector,[9] so one approach is to normalize each pixel by the maximum intensity of that pixel in the spectrum, $I(i,j,\lambda) = I(i,j,\lambda)/\max_\lambda I(i,j,\lambda)$. This makes each pixel a value between 0 and 1, and these spectra may be averaged to produce an average normalized spectra, shown as the blue line in figure 3.21(b). The image at each wavelength is histogrammed and plotted together, giving a normalized spectrum density, which is a visual representation of the likelihood of a pixel having a normalized spectral value at any wavelength. Finally, in figure 3.21(c), we see the normalized spectra adopt a characteristic density curve. The spectra at different points are largely intensity independent, expect for those points with exceptionally low postcorrected intensities. These points appear to the eye as background, but they have a different spectra, shown in figure 3.22. These spectra are likely forward scattered autofluorescence, because they most occur in the regions between somites. Autofluorescence is not uniformly distributed throughout the fish. SHG and autofluorescence are largely mutually exclusive (see figure 3.3).

Although an equivalent slice from a morphant fish, figure 3.23(a), produces substantially less SHG than the wildtype, the overall spectra shares many characteristics with the wildtype spectra. The normalized intensities still have a substantial drop-off at 850 nm, seen in figure 3.23(b), but the spectra of the morphant have a less

[9]For example, agarose density variations will alter the transparency; The position of the fish in the sample well will affect the focusing and the resulting transmission to the detector; The condenser lens must be readjusted for each sample, and it can only focus on a single plane, reducing collection efficiency for nonoptimal planes; etc.

pronounced plateau in the wavelengths shorter than 850 nm. Because the morphant contains many morphological similarities with the wildtype, we expect the spectra to be similar, due to the phase-matching being consistent (see section 4.2.2). However, the spectra of a few points of interest plotted in figure 3.23(c) differ significantly from the trend in figure 3.21(c). These points were selected from regions with lower intensity, and therefore have a character closer to figure 3.22. A background spectrum was estimated by measuring the signal from regions outside the somites, which should be nearly SHG-free. Subtracting this spectrum gives figure 3.23(d), revealing that the morphant spectrum absent the estimated background, remains very similar to the wildtype spectrum. Based on this preliminary analysis, there is no quantifiable spectral difference between 5-day-old morphants and 5-day old wildtypes. Clear morphological differences exist, such as visible tears and significantly lower conversion efficiency due to poor alignment of the myofibrils. A future experiment with fluorescently labeled myosin (or actin) would help to determine if there is myosin in the morphant which is too disrupted to produce SHG.

To explain the difference in intensity but similarity in spectral shape between wildtype and morphant zebrafish muscle, we must construct a theoretical framework for second harmonic generation. We also have seen that there are features such as the herringbones (Figs 3.14 and 3.18) that are not observed in fluorescence microscopy, which we hope to explain as well. Ultimately, second harmonic generation proves to be a valuable tool for imaging and studying muscle development and organization *in vivo* without the need for any dyes or stains. The next chapter will explore the theo-

retical aspects to SHG from zebrafish muscle and will further address the observations revealed in the present chapter.

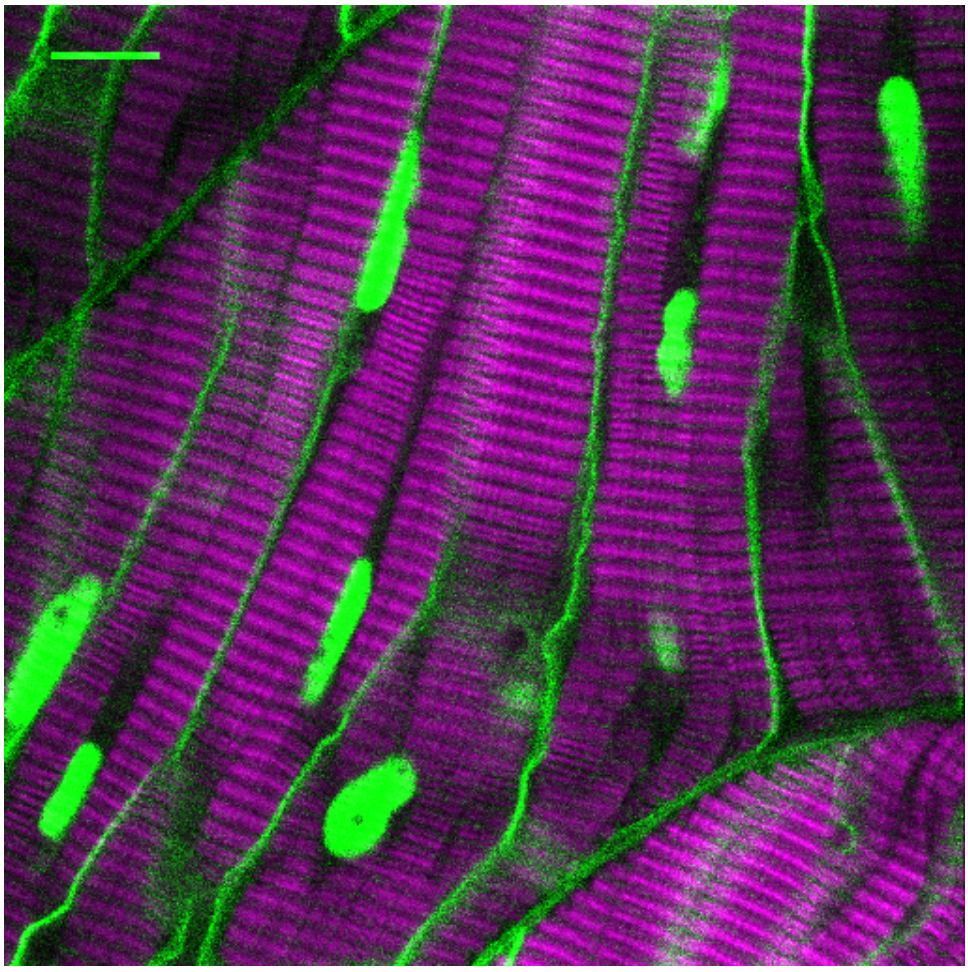

(a) sagittal plane

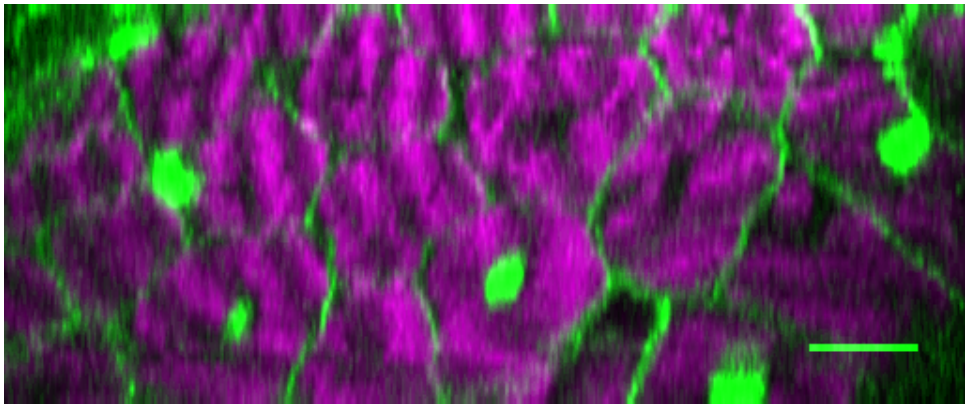

(b) transverse plane

Figure 3.17: Transgenic fish were used to visualize the interface between myofibril SHG (purple) and fluorescent-protein labeled membranes and nuclei (green). (a) Myocytes run in and out of the imaging plane, and myofibrils within a myocyte vary in their packing density and degree of contraction. (b) A perpendicular cut through the same image, showing the semi-crystalline packing of myocytes. The resolution in (b) does not allow one to resolve individual myofibrils. Scale bars are 10 μm.

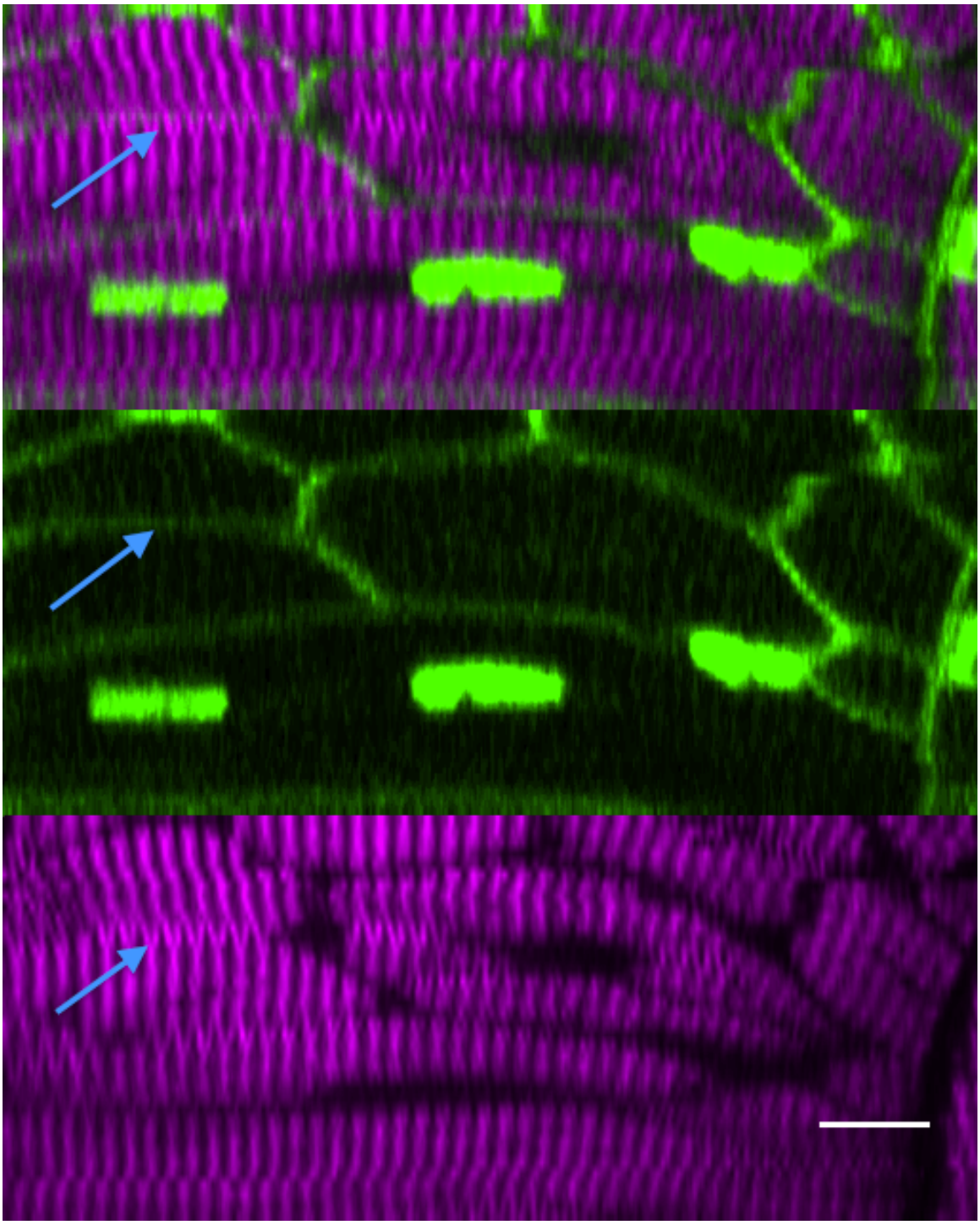

Figure 3.18: Membrane-labeled wildtype zebrafish. Bottom, SHG in purple. Middle, fluorescent membranes and nuclei in green. Top, overlay showing SHG patterns apparently crossing the membrane, which must be an optical artifact, because the myosin filaments align perpendicularly to the SHG stripes. Scale bar is 10 microns. The arrows are guides for the eye, indicating just one example where the pattern appears to cross the membrane.

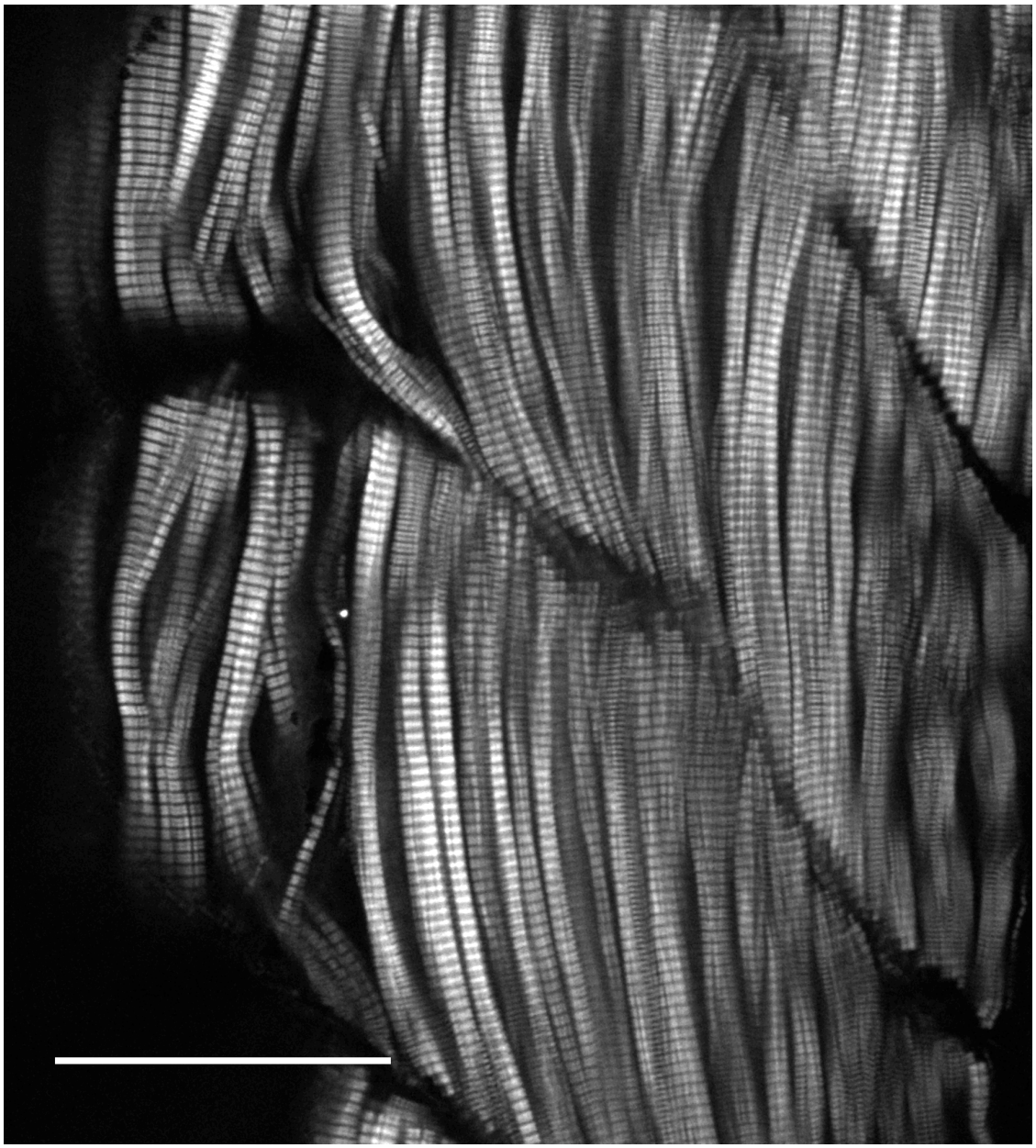

Figure 3.19: Second harmonic generation from zebrafish morphant muscle. Section along sagittal plane. The bright dot left of center appears to be a muscle fragment running perpendicular to the imaging plane, ascertained by optical sectioning (not shown). Scale bar is 50 microns

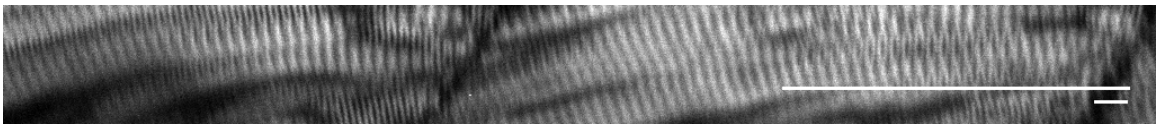

(a) wildtype

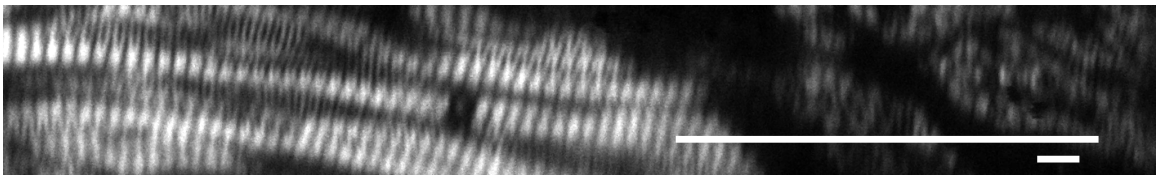

(b) morphant

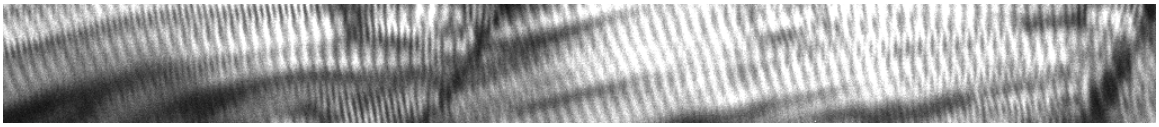

(c) wildtype - raw data

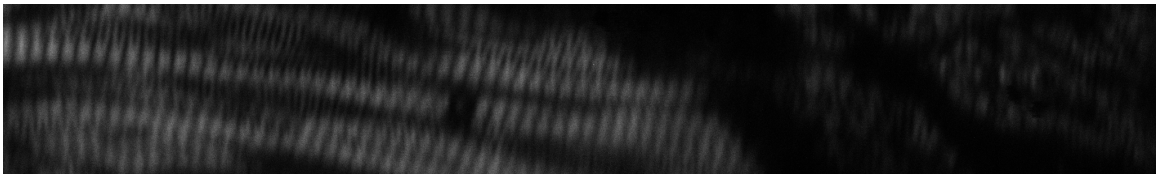

(d) morphant - raw data

Figure 3.20: Comparison of sagittal sections between (a) wildtype and (b) morphant. The morphant is much dimmer, as well as being less densely packed with muscle. Note the disrupted patterns on the right side of (b), evidence of the structural degradation due to the induced muscular dystrophy. (c) and (d) are identical images to (a) and (b), but without any brightness-contrast adjustments, to illustrate the intensity difference between the wildtype and morphant muscle. However, (a) is taken at 890 nm, while (c) and (b)/(d) are taken at 860 nm. Saturation in (c) makes visual comparison of morphology difficult. The average intensity of (c) is 18,668, including saturated pixels. The average intensity of (d) is 7,493. Long scale bar is 50 microns. Short scale bar is 5 microns.

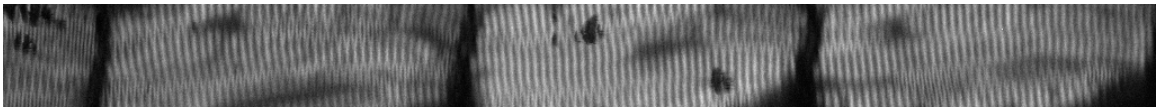

(a) 5-day wildtype coronal section

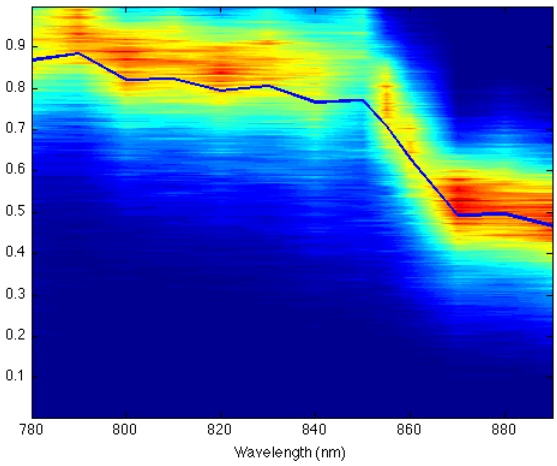

(b) SHG intensity density map

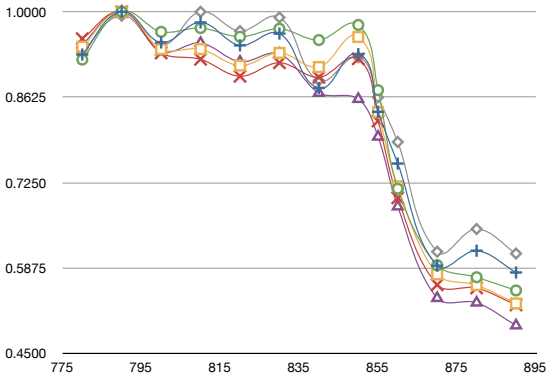

(c) Normalized spectra from representative points

Figure 3.21: The wavelength dependent SHG detected from a single sagittal plane of 5-day old zebrafish, shown in (a), shows a marked drop-off at 850 nm. (b)The density map indicates that the vast majority of spectra display a characteristic behavior. The blue line is the average of normalized spectra, and (c) sampled spectra from a few representative points illustrates their similarity. The black spots in (a) are laser ablation damage, but they do not alter the spectra of neighboring muscle.

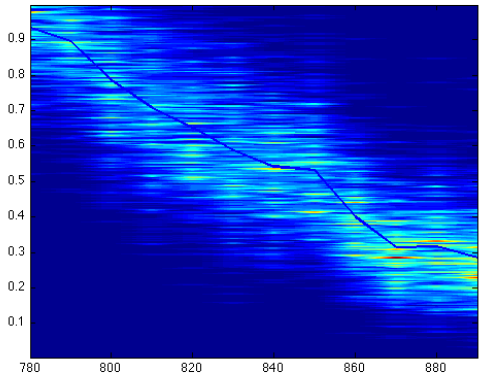

Figure 3.22: Normalized intensity spectrum density map of points from figure 3.21 of low-intensity background points.

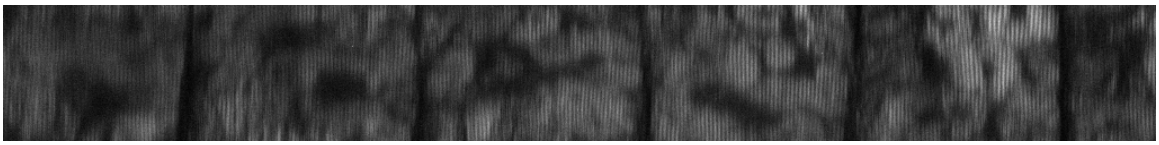

(a) 5-day morphant coronal section

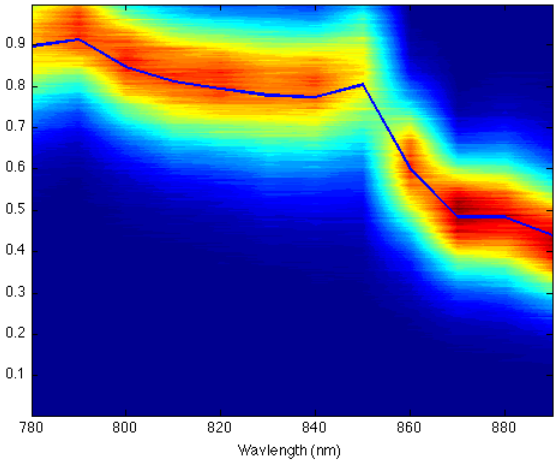

(b) SHG intensity density map

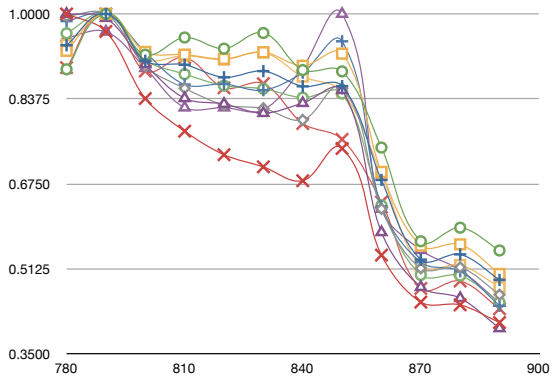

(c) Normalized spectra from representative points, both dim and bright

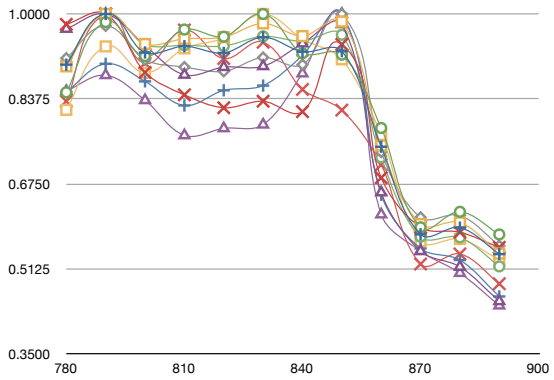

(d) Representative points with subtracted background

Figure 3.23: The wavelength dependent SHG detected from a single coronal plane of 5-day old morphant zebrafish, shown in (a), shares the drop-off at 850 nm with the wildtype spectra (figure 3.21). (b) The characteristic spectra of the morphant differs slightly. The blue line is the average of normalized spectra, and (c) sampled spectra from a few representative points. (d) The same representative points but subtracting an estimated background spectrum.